

VVDS-SWIRE \star

Clustering evolution up to $z = 2$ of a spectroscopic sample of galaxies selected from Spitzer IRAC $3.6\mu\text{m}$ and $4.5\mu\text{m}$ photometry

S. de la Torre¹, O. Le Fèvre¹, S. Arnouts¹, L. Guzzo², D. Farrah³, A. Iovino², C.J. Lonsdale^{4,5}, B. Meneux^{2,6}, S.J. Oliver⁷, A. Pollo^{1,21}, I. Waddington⁷, D. Bottini⁶, F. Fang¹⁰, B. Garilli⁶, V. Le Brun¹, D. Maccagni⁶, J.P. Picat¹³, R. Scaramella^{9,18}, M. Scovoglio⁶, D. Shupe⁴, J. Surace¹⁰, L. Tresse¹, G. Vettolani⁹, A. Zanichelli⁹, C. Adami¹, S. Bardelli⁸, M. Bolzonella⁸, A. Cappi⁸, S. Charlot^{14,15}, P. Ciliegi⁸, T. Contini¹³, S. Foucaud²⁶, P. Franzetti⁶, I. Gavignaud¹⁷, O. Ilbert²⁵, H.J. McCracken^{15,16}, B. Marano¹², C. Marinoni²³, A. Mazure¹, R. Merighi⁸, S. Paltani^{20,21}, R. Pellò¹³, L. Pozzetti⁸, M. Radovich¹¹, G. Zamorani⁸, E. Zucca⁸, M. Bondi⁹, A. Bongiorno¹², J. Brinchmann²⁴, O. Cucciati^{2,19}, F. Lamareille¹², Y. Mellier^{15,16}, P. Merluzzi¹¹, S. Temporin², D. Vergani⁶, and C.J. Walcher¹

(Affiliations can be found after the references)

Received ... / Accepted ...

ABSTRACT

Aims. By combining the VIMOS VLT Deep Survey (VVDS) with the Spitzer Wide-area InfraRed Extragalactic survey (SWIRE) data, we have built the currently largest spectroscopic sample of galaxies selected in the rest-frame near-infrared. In particular, we have obtained 2040 spectroscopic redshifts for a sample of galaxies with a magnitude measured at $3.6\mu\text{m}$ ($m_{3.6}$)_{AB} < 21.5, and 1255 spectroscopic redshifts for a sample of galaxies with ($m_{4.5}$)_{AB} < 21. These allow us to investigate, for the first time using spectroscopic redshifts, the clustering evolution of galaxies selected from their rest-frame near-infrared luminosity, in the redshift range $0.2 < z < 2.1$.

Methods. We use the projected two-point correlation function $w_p(r_p)$ to study the three dimensional clustering properties of galaxies detected at $3.6\mu\text{m}$ and $4.5\mu\text{m}$ with the InfraRed Array Camera (IRAC) in the SWIRE survey with measured spectroscopic redshifts from the first epoch VVDS. In addition, we measure the clustering properties of a larger sample of 16672 SWIRE galaxies for which we have accurate photometric redshifts on the same field by computing the angular correlation function, and we compare these measurements.

Results. We find that in the flux limited samples at $3.6\mu\text{m}$ and $4.5\mu\text{m}$, the clustering length does not change from redshift ~ 2 to the present. In addition, we find that the clustering lengths are systematically higher when galaxy samples are selected from increasingly redder wavelengths. The measured clustering lengths have a mean value around $r_0 \simeq 3.9 \text{ } h^{-1} \text{ Mpc}$ for the galaxies selected at $3.6\mu\text{m}$ and a mean value of $r_0 \simeq 4.4 \text{ } h^{-1} \text{ Mpc}$ for the galaxies selected at $4.5\mu\text{m}$, all across the redshift range explored. These values are larger than the typical values found for I-band selected galaxies in the same redshift range, but we find that the difference in clustering length between I-band and $3.6 - 4.5\mu\text{m}$ selected samples is decreasing with increasing redshift to become comparable at $z \simeq 1.5$. We interpret this as evidence that galaxies with older stellar populations and galaxies actively forming stars reside in comparably overdense environments at epochs earlier than $z \simeq 1.5$, supporting the recently reported flattening of the color-density relation at high redshift. The increasing difference in clustering length observed between rest-frame UV-optical and infrared selected samples could then be an indication that star formation is gradually shifting to lower density regions as cosmic time increases, while the older passively evolving galaxies trace the location of the highest primordial peaks.

Key words. Cosmology: observations – Cosmology: large scale structure of Universe – Galaxies: evolution – Galaxies: high-redshift – Galaxies: statistics – Infrared: galaxies

1. Introduction

Send offprint requests to: S. de la Torre, e-mail: sylvain.delatorre@oamp.fr

\star Based on data obtained with the European Southern Observatory Very Large Telescope, Paranal, Chile, program 070.A-9007(A), and on data obtained at the Canada-France-Hawaii Telescope, operated by the CNRS of France, CNRC in Canada and the University of Hawaii, and observations obtained with MegaPrime/MegaCam, a joint project of CFHT and CEA/DAPNIA, at the Canada-France-Hawaii Telescope (CFHT) which is operated by the National Research Council (NRC) of Canada, the Institut National des Science de l'Univers of the Centre National de la Recherche Scientifique (CNRS) of France, and the University of Hawaii. This work is based in part on data products produced at TERAPIX and the Canadian Astronomy Data Centre as part of the Canada-France-Hawaii Telescope Legacy Survey, a collaborative project of NRC and CNRS.

According to the current paradigm, the formation of large scale structures can be described as the evolution of primordial dark matter dominated mass density perturbations, under the influence of gravity. Galaxies we observe are the result of the cooling and fragmentation of residual gas within the potential wells provided by the dark matter halos, that hierarchically build-up with gravity (White & Rees 1978). One then expects that the spatial distribution of galaxies would trace the overall mass density field, although if galaxy formation is in some way modulated by large-scale perturbations, they will be *biased* with respect to the mass (Kaiser 1984). We have now strong observational evidence that the space distribution of galaxies is a biased estimator of the underlying mass (Bardeen et al. 1987; Lahav et al. 1989; Postman et al. 1992; Dalton et al. 1994; Croft et al. 1997;

Gonzalez et al. 2002) and the study of galaxy clustering as a function of different galaxy properties may allow us to understand the evolution of the galaxy-halo bias. As galaxies and their environment evolve, clustering may evolve and because of the different physical processes that may be involved in building different classes of galaxies, its strength may depend on the properties of galaxies (e.g. type, luminosity...) and their environment. The clustering evolution of different galaxy populations could therefore provide useful constraints on the evolution and formation scenario of galaxies.

When galaxies are observed from redder wavelengths and up to a few microns rest-frame, this preferentially selects older stellar populations formed earlier in the life of the Universe. As the oldest stars are likely to have formed in the highest density peaks in the Universe, it is therefore expected that the clustering of their host galaxies would be significantly higher than that of galaxies hosting more recently formed stars. In the local Universe, selecting galaxies at 2.15 microns (K_s band) from the Two Micron All Sky Survey (2MASS, Maller et al. 2005), it is found that these galaxies are more clustered than those selected at optical wavelengths, with an angular correlation amplitude 7.7 times larger than found in the Sloan Digital Sky Survey Early Data Release (SDSS EDR, Connolly et al. 2002), note that in the 2MASS analysis, the galaxies are selected according to the magnitude criterion $(K_s)_{Vega} < 13.57$ and in the SDSS EDR study they select galaxies ~ 2 magnitudes fainter. Getting to higher redshifts, Oliver et al. (2004), based on Spitzer data, found that at $z_{median} \simeq 0.75$ the clustering length of $(m_{3.6})_{AB} < 20.1$ galaxies is $r_0 = 4.4 \pm 0.1 h^{-1} Mpc$ with an angular correlation amplitude ~ 5.9 times lower than for 2MASS local galaxies, and the more luminous galaxies are even more strongly clustered (Farrah et al. 2006). As selection wavelengths get redder than the rest-frame location of polycyclic aromatic hydrocarbon (PAH) spectral features, galaxy samples contain a mix of early-type, dust-reddened, and star-forming systems (Rowan-Robinson et al. 2005), hence, clustering expectations are less straightforward.

This paper aims to characterize the evolution of the real-space correlation length r_0 of near-infrared selected galaxies from the Spitzer Wide-area InfraRed Extragalactic survey (SWIRE, Lonsdale et al. 2003) which have secure spectroscopic redshifts from the VIMOS VLT Deep Survey (VVDS, Le Fèvre et al. 2005b) and to compare it to the observed evolution of optically-selected galaxies as shown in Le Fèvre et al. (2005a), up to $z \simeq 2$.

In Section 2 we describe the galaxy sample and its selection function. We present in Section 3 the formalism of the two-point correlation function and the results. In Section 4 we discuss the observed clustering evolution and we conclude.

Throughout this analysis we assume a flat ΛCDM cosmology with $\Omega_M = 0.3$, $\Omega_\Lambda = 0.7$ and $H_0 = 100 h^{-1} km \cdot s^{-1} \cdot Mpc^{-1}$, while a value of $H_0 = 70 km \cdot s^{-1} \cdot Mpc^{-1}$ is used when computing absolute magnitudes.

2. VVDS-SWIRE samples and selection functions

The VVDS-SWIRE field is the intersection of the VIRMOS Deep Imaging Survey (VDIS, Le Fèvre et al. 2004) and the SWIRE-XMM/LSS fields, the total area covered on the sky is $\sim 0.82 deg^2$. From this field we extract two galaxy samples.

The larger one consists of those SWIRE galaxies present in the field for which we measured photometric redshifts, therefore we will call this sample the photometric redshift sample. The photometric redshifts have been computed using a χ^2 fitting algorithm

as described in Ilbert et al. (2006) by including all the photometric information available for this field, covering the wavelength domain $0.31 \mu m \leq \lambda \leq 5.0 \mu m$. Thus the photometric data consist in B,V,R,I data from VDIS (Le Fèvre et al. 2004), u^*,g^*,r^*,i^*,z^* data from the Canada France Hawaii Telescope Legacy Survey (CFHTLS-D1, McCracken et al., in preparation), K-band data from VDIS (Iovino et al. 2005) adding the $3.6 \mu m$ and $4.5 \mu m$ infrared photometry from SWIRE (Lonsdale et al. 2003). The details of the method used to compute the photometric redshifts are given in Arnouts et al. (2007, in preparation).

The other sample, hereafter the spectroscopic redshift sample, contains the galaxies included in a sub-area of $\sim 0.42 deg^2$ which correspond to a fraction of the VVDS-Deep survey (Le Fèvre et al. 2005b) area and for which we have spectroscopic redshifts measured during the VVDS first epoch observations. We restrict this sample to galaxies with secure redshifts, i.e. with redshift confidence level greater than 80% (flag 2 to 9, Le Fèvre et al. 2005b).

The samples have been split into two subsamples, applying a simple magnitude selection from observed fluxes on the two first infrared photometric bands of the SWIRE survey, the Spitzer-IRAC $3.6 \mu m$ and $4.5 \mu m$ bands. The subsamples satisfy respectively to the following magnitude criteria: a magnitude in the AB system measured in the $3.6 \mu m$ band of $(m_{3.6})_{AB} < 21.5$ and in the $4.5 \mu m$ band of $(m_{4.5})_{AB} < 21$ or equivalently in flux, $S_{3.6} > 9.2 \mu Jy$ and $S_{4.5} > 14.5 \mu Jy$. These correspond to the limits of completeness for the SWIRE bands (Le Fèvre et al., 2007, in preparation). In addition, the spectroscopic redshift sample has a I_{AB} cut due to the fact that the VVDS-Deep spectroscopic sample is a magnitude-selected sample according to the criterion $17.5 \leq I_{AB} \leq 24$. The I_{AB} cut introduces a color dependent incompleteness in terms of SWIRE magnitudes in the spectroscopic redshift sample, indeed we lose a small fraction of objects which correspond to faint and red objects as shown in Figure 1 for the $3.6 \mu m$ galaxies. The equivalent color-magnitude diagram for the $4.5 \mu m$ galaxy sample is similar to the $3.6 \mu m$ one, the two spectroscopic redshift subsamples have a similar kind of incompleteness. We estimate the fraction of lost galaxies to be respectively 11.6% and 10.3% for the $3.6 \mu m$ and $4.5 \mu m$ spectroscopic redshift subsamples. Thus, the photometric redshift sample, which is assumed to be complete, allow us to evaluate the effect of the color dependent magnitude incompleteness on the clustering measurements performed on the spectroscopic redshift sample. A full description of the combined dataset and its properties is given in Le Fèvre et al. (2007, in preparation).

3. Clustering measurements

3.1. Methods

3.1.1. Computing the projected correlation function

The method applied to compute the projected correlation function (PCF) and to derive the real-space correlation length r_0 and the correlation function slope γ , is described extensively in Pollo et al. (2005). We present in this section the main points of the method.

First we evaluate the bi-dimensional two-point correlation function $\xi(r_p, \pi)$ using the standard Landy and Szalay estimator (Landy & Szalay 1993). This estimator of the two-point correlation function is defined by:

$$\xi(r) = \frac{GG(r) - 2GR(r) + RR(r)}{RR(r)} \quad (1)$$

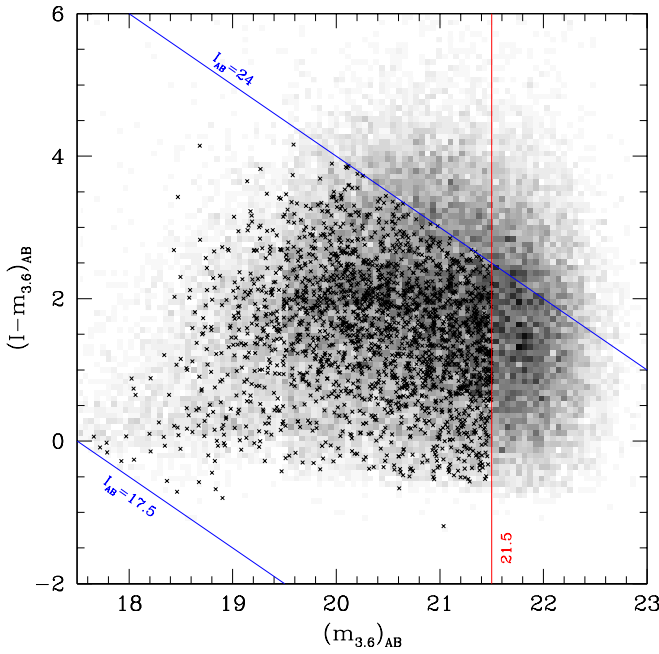


Fig. 1. Color-magnitude diagram for the $3.6\mu\text{m}$ spectroscopic and photometric subsamples. All the galaxies detected at $3.6\mu\text{m}$ in the VVDS-SWIRE field are represented in greyscale. The photometric redshift subsample consists of all the objects with $(m_{3.6})_{AB} < 21.5$ and galaxies from the spectroscopic subsample are shown as crosses. The vertical line indicates the limit of completeness and the two diagonal lines show the limits of the spectroscopic selection $17.5 \leq I_{AB} \leq 24$. We estimate that the percentage of galaxies that we lose in the spectroscopic redshift subsample due to the VVDS spectroscopic selection and assuming the completeness limit $(m_{3.6})_{AB} < 21.5$, is 11.6%.

where $GG(r)$, $RR(r)$ and $GR(r)$ are the normalized numbers of independent galaxy-galaxy, galaxy-random and random-random pairs with comoving separation between r and $r + dr$. The three-dimensional galaxy space distribution recovered from a redshift survey and its two-point correlation function $\xi(s)$, are distorted due to the effect of galaxy peculiar velocities, therefore, the redshift-space separation s differs from the true physical comoving separation r . These distortions occur only radially since peculiar velocities affect only redshift. Thus we compute the bi-dimensional two-point correlation $\xi(r_p, \pi)$ by splitting the separation vector s into two components: r_p and π , respectively perpendicular and parallel to the line of sight (Fisher et al. 1994). In this way, we separate the redshift distortions from the true spatial correlations.

Then, we project $\xi(r_p, \pi)$ along the line of sight, onto the r_p axis. This allows to integrate out the dilution produced by the redshift-space distortion field and thus we obtain the projected two-point correlation function, which is defined as,

$$w_p(r_p) = 2 \int_0^\infty \xi(r_p, \pi) d\pi = 2 \int_0^\infty \xi\left(\sqrt{r_p^2 + y^2}\right) dy \quad (2)$$

In practice, the upper integration limit has to be chosen finite, therefore we choose its optimal value as $20 h^{-1} \text{Mpc}$ (Pollo et al.

2005). Assuming a power-law form for $\xi(r)$, i.e. $\xi(r) = (r_0/r)^\gamma$, one can write $w_p(r_p)$ as,

$$w_p(r_p) = r_p \left(\frac{r_0}{r_p}\right)^\gamma \frac{\Gamma\left(\frac{1}{2}\right) \Gamma\left(\frac{\gamma-1}{2}\right)}{\Gamma\left(\frac{\gamma}{2}\right)} \quad (3)$$

where Γ is the Euler Gamma function.

Fitting the $w_p(r_p)$ measurements by minimizing the generalized χ^2 as defined in Pollo et al. (2005), provides a measurement of r_0 and γ . This minimization method takes into account the fact that the different points of the correlation function are not independent. The estimate of errors is performed primarily using the bootstrap resampling method. This first error measurement permits to obtain a relatively good fitting of measured $w_p(r_p)$. Then we compute $w_p(r_p)$ on 50 mock VVDS surveys constructed using the GalICS simulations (Blaizot et al. 2005) in order to obtain a realistic estimation of the errors bars on the measurements which include the error due to cosmic variance. Indeed, these mock samples include the same selection function and observational biases present in the VVDS dataset and permit to evaluate the confidence limits on r_0 and γ measurements (Pollo et al. 2005).

3.1.2. Computing the angular correlation function

In order to compute the angular two-point correlation function $w(\theta)$ (ACF), we use the Landy & Szalay estimator presented in equation 1, but in this case, simply considering angular pairs. Assuming that $w(\theta)$ is well described by a power law model as $w(\theta) = A_w \theta^{1-\gamma}$, we fit this model to the measured ACF using the generalized χ^2 method. Thus we deduce the amplitude A_w and the slope $1 - \gamma$ of the ACF. We introduce the integral constraint (IC) correction in our fitting procedure, which arises from the fact that the survey has a finite size. It is defined as follows (Roche et al. 1993),

$$IC = \iint \frac{w(\theta)}{\Omega^2} d\Omega_1 d\Omega_2 = \frac{A_w}{\Omega^2} \iint \theta^{1-\gamma} d\Omega_1 d\Omega_2 = A_w B(\gamma) \quad (4)$$

with,

$$B(\gamma) = \frac{1}{\Omega^2} \iint \theta^{1-\gamma} d\Omega_1 d\Omega_2 \quad (5)$$

where Ω is the area of the observed field. We compute $B(\gamma)$ by numerically integrating this expression over the entire data area excluding regions where there are photometric defects. At the end our measurements are fitted with the expression:

$$w_{mod}(\theta) = A_w \theta^{1-\gamma} - IC = A_w (\theta^{1-\gamma} - B(\gamma)) \quad (6)$$

In order to derive the real-space correlation length r_0 from the angular correlation amplitude A_w , we use the Limber deprojection technique as described in Magliocchetti & Maddox (1999). This method, which is based on the Limber relativistic equation (Limber 1953), permits to recover the value of r_0 given A_w and the redshift distribution of the galaxies. In general, this technique is not very stable and the shape of the redshift distribution that one considers is critical, but in this study, we measure ACF in relatively narrow redshift bins so the shape we assume for the inversion is not so critical. Hence, we use a smoothed redshift distribution by applying a moving window with a width of $\Delta z = 0.2$ to the initial photometric redshift distribution (Le Fèvre et al., 2007, in preparation). The width of the smoothing window has been chosen to reflect the typical uncertainty that we have on the photometric redshift values. ACF error bars have been computed using the bootstrap resampling method.

Table 1. VVDS-SWIRE spectroscopic redshift sample: subsample properties and associated measurements of the slope and the correlation length.

Spectroscopic redshift sample							
Subsample	Redshift interval	Median redshift	Number of galaxies	Median M_B (Vega system)	γ	$r_0 (h^{-1} \text{ Mpc})$	$r_0 (h^{-1} \text{ Mpc})$ (fixed $\gamma = 1.8$)
3.6 μm	[0.2, 0.5]	0.36	336	-19.53	$1.92^{+0.27}_{-0.18}$	$3.8^{+0.6}_{-0.7}$	$3.9^{+0.6}_{-0.7}$
	[0.5, 0.7]	0.60	445	-20.29	$1.88^{+0.21}_{-0.14}$	$4.2^{+0.5}_{-0.5}$	$4.4^{+0.5}_{-0.5}$
	[0.7, 0.9]	0.81	512	-20.75	$1.77^{+0.15}_{-0.15}$	$3.8^{+0.4}_{-0.4}$	$3.7^{+0.4}_{-0.4}$
	[0.9, 1.1]	0.99	385	-21.17	$1.87^{+0.11}_{-0.14}$	$4.2^{+0.4}_{-0.4}$	$4.3^{+0.4}_{-0.4}$
	[1.1, 1.3]	1.19	195	-21.66	$2.44^{+0.22}_{-0.16}$	$3.8^{+0.5}_{-0.5}$	$3.7^{+0.5}_{-0.5}$
	[1.3, 2.1]	1.57	93	-22.13	$2.19^{+0.39}_{-0.38}$	$5.8^{+0.5}_{-1.0}$	$7.6^{+0.7}_{-1.0}$
4.5 μm	[0.2, 0.7]	0.48	485	-20.22	$1.84^{+0.18}_{-0.16}$	$3.9^{+0.5}_{-0.5}$	$3.9^{+0.5}_{-0.5}$
	[0.7, 1.1]	0.90	537	-21.15	$1.84^{+0.14}_{-0.14}$	$4.0^{+0.3}_{-0.4}$	$4.0^{+0.3}_{-0.4}$
	[1.1, 2.1]	1.42	182	-21.97	$1.82^{+0.26}_{-0.22}$	$3.7^{+0.6}_{-0.7}$	$3.7^{+0.6}_{-0.7}$

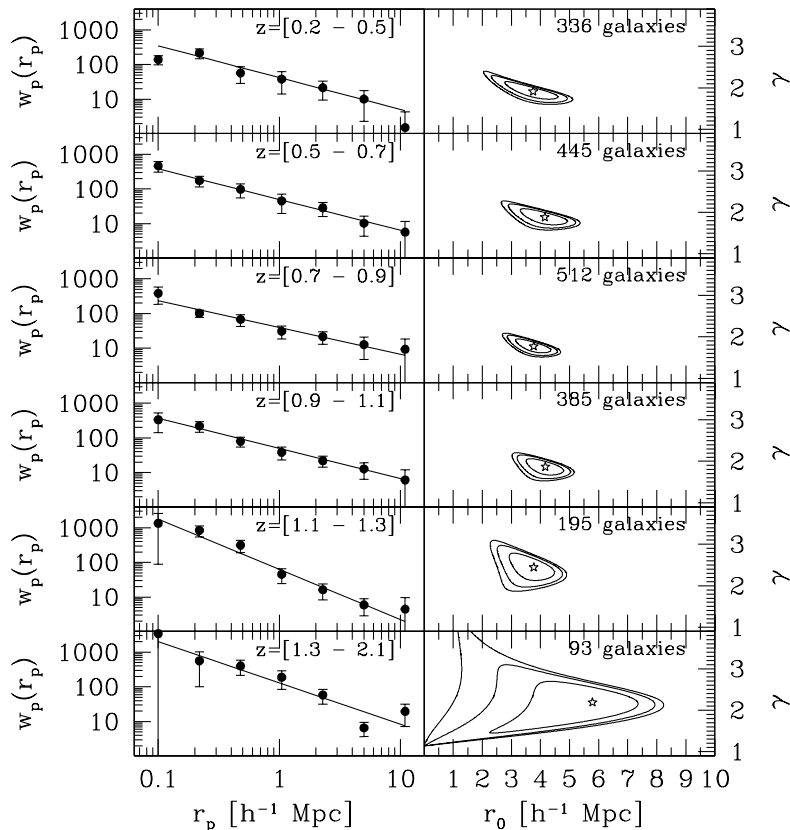


Fig. 2. In the left panels are shown the projected correlation functions for the 3.6 μm spectroscopic redshift subsample in the different redshift slices and their best-fits. The right panels shows the 68.3%, 90% and 95.4% confidence contours for the clustering parameters r_0 and γ .

3.2. Clustering results

3.2.1. Clustering of the spectroscopic redshift sample

We compute $w_p(r_p)$ in increasing spectroscopic redshift slices from $z = 0.2$ to $z = 2.1$. Therefore we divide the 3.6 μm subsample in six redshift slices: [0.2, 0.5], [0.5, 0.7], [0.7, 0.9], [0.9, 1.1], [1.1, 1.3], [1.3, 2.1]. The 4.5 μm subsample has less objects than the 3.6 μm one because of the slightly shallower depth, and in order to maximize the number of objects, we reduce the number of slices to three, considering [0.2, 0.7], [0.7, 1.1] and [1.1, 2.1].

In the fitting procedure, we use all the $w_p(r_p)$ points for $0.1 \leq r_p \leq 12 h^{-1} \text{ Mpc}$. The PCF that we compute for each redshift slice are plotted in Figure 2 with the contours of confidence for the best-fitted parameters. The Table 1 summarizes the values of the correlation length and the correlation function slope that we derive for the two subsamples of the spectroscopic redshift sample.

The correlation length that we measure in the 3.6 μm and 4.5 μm subsamples is roughly constant over the redshift range $z=[0.2, 2.1]$, it varies slightly between 3.8 and 4.2 $h^{-1} \text{ Mpc}$, except in the last high-redshift interval [1.3, 2.1] of the 3.6 μm subsample where we measure a large correlation length

of $5.8 h^{-1} \text{ Mpc}$. In this case we select preferentially the intrinsically brightest galaxies of the subsample, as shown in Table 1 the median absolute magnitude of these galaxies is $< M_B > = -22.13$. These very luminous galaxies are expected to be strongly clustered with r_0 values greater than $5 h^{-1} \text{ Mpc}$ (Pollo et al. 2006; Farrah et al. 2006) and this is consistent with our results. Indeed, this redshift interval contains the $1.6\mu\text{m}$ rest-frame emission feature which arises due to the photospheric emission from evolved stars (Simpson & Eisenhardt 1999), picking-up in the $3.6\mu\text{m}$ band, more massive and significantly more clustered systems (Farrah et al. 2006). We discuss in details the evolution of the correlation length that we measure for the two subsamples in Section 4.

3.2.2. Clustering of the photometric redshift sample

We measure the ACF and deduce the clustering parameters r_0 and γ on the photometric redshift sample in order to test the spectroscopic redshift sample measurements and to evaluate the incompleteness effect.

With the same methodology we compute the ACF in increasing photometric redshift slices, selecting the slice boundaries in order to take into account the photometric redshift error $\sigma \simeq 0.03(1+z)$ (Arnouts et al. 2007, in preparation). Therefore we consider five photometric redshift slices with an increasing size: $[0.2, 0.5]$, $[0.5, 0.7]$, $[0.7, 1.0]$, $[1.0, 1.3]$ and $[1.3, 1.7]$. No redshift slices have been considered beyond $z_{\text{phot}} = 1.7$ because the lack of accuracy of the photometric redshifts in this case corrupts seriously the measurements.

We fit the power law model to the measured ACF over $0.0017 \leq \theta \leq 0.1$ degrees, indeed in this region the shape of the ACF is very close to a power law. However, one can see clearly that the ACF departs from this model at scales greater than ~ 0.1 degrees in the redshift slices greater than $z_{\text{phot}} = 0.7$ (Figure 3). This excess of power at large angular scale could be explained by the presence of another component in the correlation function or of the presence of residual inhomogeneities in the field. We will explore this point more in detail in a future paper as it does not impact the results presented in this paper. The ACF that we compute for the different redshift slices are plotted in Figure 3. In Table 2 is reported the best-fitted values of the angular correlation amplitude A_w , the correlation function slope γ and the correlation length r_0 that we derive with the Limber deprojection technique.

Given the uncertainties on the ACF measurements, we have adopted a fixed slope of $\gamma = 1.8$ to minimize the errors in computing the correlation length r_0 . This is supported by the fact that when letting both r_0 and γ vary in the ACF fitting, we find γ values very similar to 1.8, while errors on r_0 slightly increase.

The values of the correlation length that we derive for the $3.6\mu\text{m}$ and $4.5\mu\text{m}$ photometric samples do not evolve with redshift up to $z_{\text{phot}} = 1.7$. In the case of the $3.6\mu\text{m}$ subsample, the r_0 values are in good agreement with the values found in the spectroscopic redshift sample given the size of the error bars. Comparing the measurements at $4.5\mu\text{m}$, we observe systematically larger values of the correlation length for the $4.5\mu\text{m}$ photometric redshift subsample than for the $4.5\mu\text{m}$ spectroscopic redshift one. We interpret the difference in the r_0 values between the two samples as an effect of the incompleteness. The fact that the incompleteness of the spectroscopic redshift sample does not influence our clustering measurements for the $3.6\mu\text{m}$ galaxies indicates that the missed population

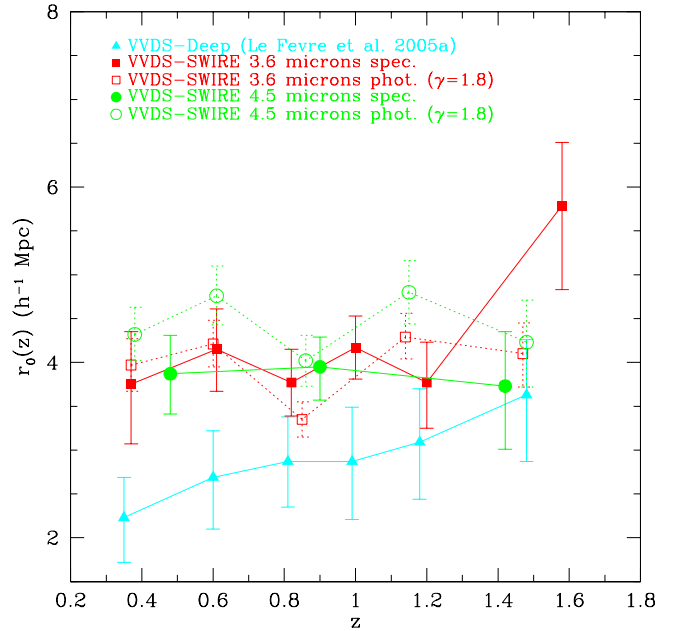


Fig. 4. Clustering evolution of VVDS-SWIRE samples of near-infrared galaxies compared to the VVDS-Deep I-band measurements.

effectively does not contribute much to the clustering signal. On the contrary the spectroscopic redshift sample underestimates the clustering at $4.5\mu\text{m}$, the missing fraction of objects in this case seems to be dominated by extremely red objects which are more clustered than the main population.

4. Discussion and conclusions

We first compare our measurements with previously reported results on samples of galaxies selected using Spitzer-IRAC bands. Oliver et al. (2004) use a similar type of galaxy selection, as they define a flux-limited sample of SWIRE galaxies with $S_{3.6} > 32\mu\text{Jy}$, and they compute the ACF and deduce r_0 using Limber deprojection assuming a parameterized redshift distribution. The selection criterion that they consider is different from the one we use, i.e. $S_{3.6} > 9.2\mu\text{Jy}$, selecting brighter galaxies than in our sample, therefore expected to be more strongly clustered (Pollo et al. 2006). Taking into account this difference and uncertainties in the redshift distribution they have assumed, the correlation length that they find is consistent with our results, they found $r_0 = 4.4 \pm 0.1 h^{-1} \text{ Mpc}$ at $z \simeq 0.75$ with $\gamma = 1.8$, which is comparable to our value $r_0 = 3.7 \pm 0.4 h^{-1} \text{ Mpc}$ in the redshift interval $z = [0.7, 0.9]$.

We then compare our results with the clustering measurements of I-band selected VVDS-Deep galaxies (Le Fèvre et al. 2005a) in the same area. This comparison is shown in Figure 4, where the correlation length for the different samples is plotted. We observe that the correlation length is globally higher for near-infrared selected galaxies compared to optically-selected ones and that it is roughly constant over the redshift range $z = [0.2, 2.1]$. By comparison, r_0 from the I-selected sample shows a steady increase with redshift. As discussed in Section 3, the clustering of the $4.5\mu\text{m}$ -selected galaxy population is higher as measured from the photometric sample than from the spectro-

Table 2. VVDS-SWIRE photometric redshift sample: subsample properties and associated measurements of the ACF amplitude, the slope and the correlation length.

Photometric redshift sample							
Subsample	Photometric redshift interval	Median redshift	Number of galaxies	$A_w \times 10^3$	γ	$r_0 (h^{-1} \text{Mpc})$	$r_0 (h^{-1} \text{Mpc})$ (fixed $\gamma = 1.8$)
3.6 μm	[0.2, 0.5]	0.37	2726	$7.7^{+4.7}_{-3.1}$	$1.76^{+0.10}_{-0.09}$	$4.2^{+1.5}_{-1.0}$	$4.0^{+0.3}_{-0.3}$
	[0.5, 0.7]	0.60	2714	$7.1^{+4.5}_{-3.0}$	$1.83^{+0.10}_{-0.09}$	$4.1^{+1.4}_{-0.9}$	$4.2^{+0.3}_{-0.3}$
	[0.7, 1.0]	0.85	5110	$1.2^{+0.8}_{-0.5}$	$2.03^{+0.11}_{-0.11}$	$2.8^{+1.0}_{-0.6}$	$3.4^{+0.2}_{-0.2}$
	[1.0, 1.3]	1.14	3577	$5.1^{+4.0}_{-2.5}$	$1.81^{+0.12}_{-0.12}$	$4.3^{+0.9}_{-1.1}$	$4.3^{+0.3}_{-0.3}$
	[1.3, 1.7]	1.47	2545	$3.4^{+3.7}_{-1.9}$	$1.83^{+0.16}_{-0.15}$	$4.0^{+2.4}_{-1.2}$	$4.1^{+0.4}_{-0.4}$
	[0.2, 0.5]	0.37	1977	$7.6^{+4.3}_{-3.8}$	$1.79^{+0.09}_{-0.09}$	$4.4^{+1.4}_{-0.9}$	$4.3^{+0.3}_{-0.3}$
	[0.5, 0.7]	0.60	1708	$10.4^{+8.5}_{-4.9}$	$1.80^{+0.13}_{-0.13}$	$4.8^{+2.2}_{-1.2}$	$4.8^{+0.3}_{-0.3}$
4.5 μm	[0.7, 1.0]	0.85	2971	$1.1^{+1.0}_{-0.5}$	$2.10^{+0.12}_{-0.13}$	$3.0^{+1.4}_{-0.7}$	$4.0^{+0.3}_{-0.3}$
	[1.0, 1.3]	1.14	2287	$6.1^{+7.1}_{-3.3}$	$1.81^{+0.15}_{-0.16}$	$4.8^{+3.1}_{-1.4}$	$4.8^{+0.4}_{-0.4}$
	[1.3, 1.7]	1.47	1700	$4.3^{+3.9}_{-2.5}$	$1.79^{+0.17}_{-0.19}$	$4.3^{+3.2}_{-1.4}$	$4.2^{+0.5}_{-0.5}$

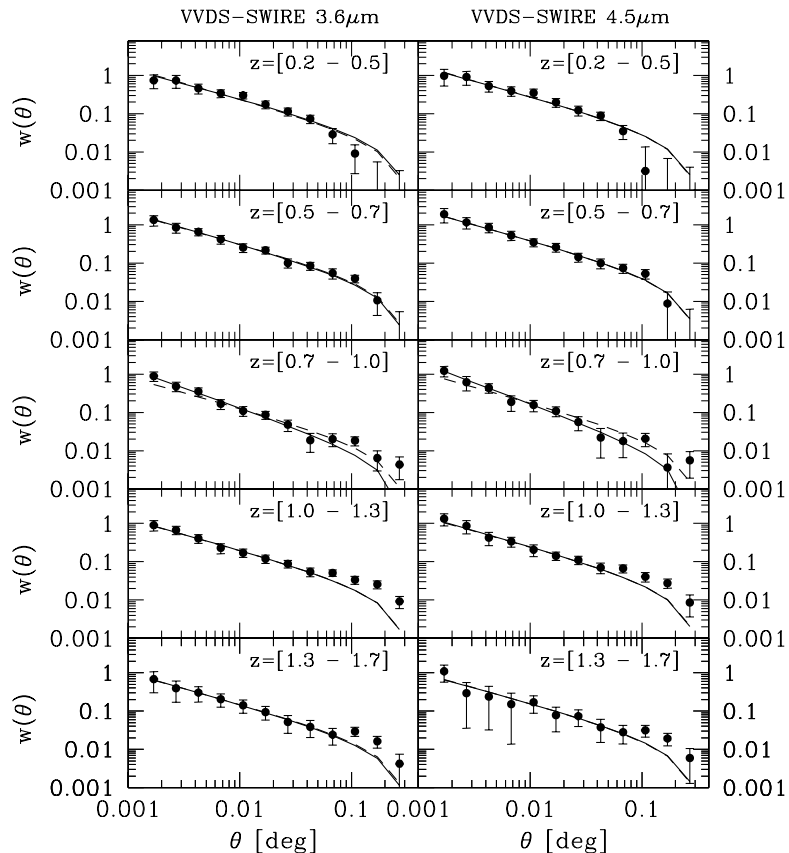


Fig. 3. These panels present the angular correlation functions as a function of redshift, for the 3.6 μm and 4.5 μm photometric redshift subsamples. The solid lines show the best-fit model when letting the two parameters free, while the dashed lines indicate the best-fit model with fixed $\gamma = 1.8$.

scopic sample because the latter misses a significant fraction of red galaxies due to the additional $17.5 \leq I_{AB} \leq 24$ cut applied by the VVDS-Deep survey selection. When comparing this measurement with the one at 3.6 μm , we therefore observe that the clustering of the sample selected at the redder wavelength is slightly stronger. This is expected as selecting from longer wavelengths is sampling slightly earlier galaxy types as described below. The color dependency of the clustering of galaxies in the VVDS-SWIRE sample will be reported elsewhere (de la Torre et al., in preparation).

In order to understand the systematically higher values of clus-

tering that we find compared to those from optically-selected galaxies and to qualify with accuracy the type of galaxy population included in our near-infrared samples, we derive the spectral types of our spectroscopic redshift sample galaxies using the galaxy classification introduced by Zucca et al. (2006). This classification is based on the match to an empirical set of spectral energy distributions (as described in Arnouts et al. 1999) of the galaxy rest-frame colors, obtained from the multi-wavelength information and spectroscopic redshift. The redshift distributions per galaxy types are presented in Figure 5 for the I-band, 3.6 μm and 4.5 μm selected samples. The four spectral types de-

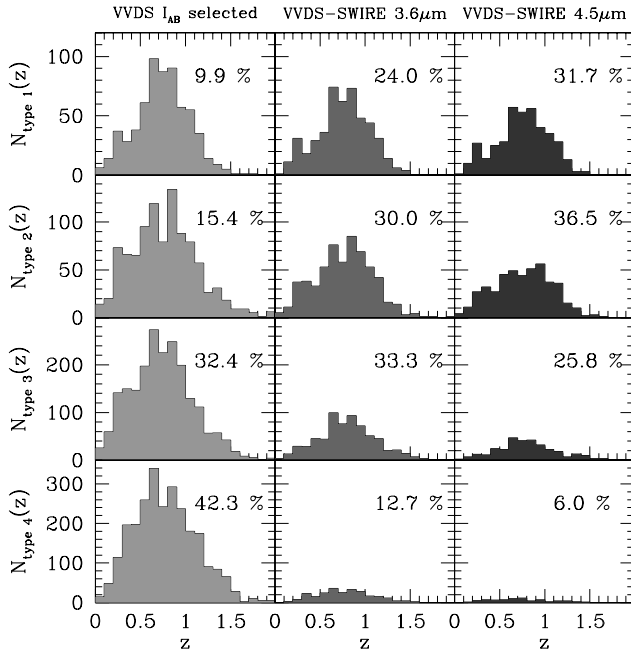


Fig. 5. Redshift distribution per spectral types for the $3.6\mu\text{m}$ and $4.5\mu\text{m}$ spectroscopic redshift subsamples compared to the VVDS-Deep sample. We use the spectral types defined in Zucca et al. (2006): type 1 corresponds to E/S0, type 2 to early spiral, type 3 to late spiral and type 4 to irregular/starburst galaxies.

fined as type 1 to 4 correspond respectively to E/S0, early spiral, late spiral and irregular/starburst galaxies. One can see in Figure 5 that the VVDS-Deep I-selected sample is dominated by late types (type 3 and 4) whereas the $4.5\mu\text{m}$ selected sample is dominated by early types (type 1 and 2). In the $3.6\mu\text{m}$ sample the different types balance out. The early type galaxies are known to be more clustered than late type ones (e.g. Norberg et al. 2002; Zehavi et al. 2005; Meneux et al. 2006), thus the proportion of early type galaxies that we found in the different samples can explain why globally we measure higher values of clustering as galaxies are selected from redder observed wavelengths, over the complete redshift range explored.

On the other hand, understanding the relatively constant clustering that we observe in our near-infrared samples is not trivial. When we select galaxies at $3.6\mu\text{m}$ or $4.5\mu\text{m}$, we are probing at any redshift in the range $0 < z < 2$, the near-infrared rest-frame of the galaxies which is more sensitive to the emission from low-mass stars. Thus our near-infrared selection is mostly driven by stellar mass, considering that luminous infrared galaxies are massive objects for which a lot of their mass is in old stars. If one considers that these galaxies are simply tracing passively the growth of clustering in the mass, one would expect the correlation length to increase with time. On the contrary, as we select more intrinsically luminous galaxies with increasing redshift because of the magnitude selection of the sample, and since more luminous galaxies are more clustered (Pollo et al. 2006), we expect to measure a higher clustering as redshift increases. We propose that these two competing effect, working simultaneously, combine to produce the roughly constant clustering amplitude with redshift that we observe.

It is particularly interesting to note that at $z \approx 1.5$, the correlation length of galaxies selected from the UV-optical rest-frame and

hence actively star-forming is very similar to that of galaxies selected in the rest-frame near-infrared dominated by older stellar populations. This is quite different from what is observed in the local Universe where selecting galaxies in the K_s band from the 2MASS survey (Maller et al. 2005), it is found that these galaxies are significantly more clustered than those selected at optical wavelengths (SDSS EDR, Connolly et al. 2002). The galaxies which are making stars at $z \approx 1.5$ therefore reside in similarly clustered regions as those containing the bulk of stellar mass, while at $z = 0$ the bulk of star formation happens in a population which is much less clustered than that where the bulk of stellar mass already resides. We interpret this as an evidence for star formation shifting from high density to low density regions, as cosmic time increases. This result is fully consistent with the observed flattening of the color-density relation above $z = 1.2 - 1.5$ (Cucciati et al. 2006), meaning that at these redshifts, star forming galaxies and older galaxies are found to reside with equal probability in high or low density regions. This can be seen as yet another manifestation of the "downsizing" trend which has been indicated by observations over the last few years (e.g. Cowie et al. 1996), and that points out the primary role of the mass in regulating star formation in galaxies (Gavazzi et al. 2002): while at high redshift star formation was strong in massive and more clustered galaxies, today it is mainly limited to lower mass galaxies more uniformly distributed.

Acknowledgements. This research has been developed within the framework of the VVDS consortium.

This work has been partially supported by the CNRS-INSU and its Programme National de Cosmologie (France), and by Italian Ministry (MIUR) grants COFIN2000 (MM02037133) and COFIN2003 (num.2003020150).

The VLT-VIMOS observations have been carried out on guaranteed time (GTO) allocated by the European Southern Observatory (ESO) to the VIRMOS consortium, under a contractual agreement between the Centre National de la Recherche Scientifique of France, heading a consortium of French and Italian institutes, and ESO, to design, manufacture and test the VIMOS instrument.

References

- Arnouts, S., Cristiani, S., Moscardini, L., et al. 1999, MNRAS, 310, 540
- Bardeen, J. M., Bond, J. R., & Efstathiou, G. 1987, ApJ, 321, 28
- Blaizot, J., Wadadekar, Y., Guiderdoni, B., et al. 2005, MNRAS, 360, 159
- Connolly, A. J., Scranton, R., Johnston, D., et al. 2002, ApJ, 579, 42
- Cowie, L. L., Songaila, A., Hu, E. M., & Cohen, J. G. 1996, AJ, 112, 839
- Croft, R. A. C., Dalton, G. B., Efstathiou, G., Sutherland, W. J., & Maddox, S. J. 1997, MNRAS, 291, 305
- Cucciati, O., Iovino, A., Marinoni, C., et al. 2006, A&A, 458, 39
- Dalton, G. B., Croft, R. A. C., Efstathiou, G., et al. 1994, MNRAS, 271, L47+
- Farrah, D., Lonsdale, C. J., Borys, C., et al. 2006, ApJ, 643, L139
- Fisher, K. B., Davis, M., Strauss, M. A., Yahil, A., & Huchra, J. P. 1994, MNRAS, 267, 927
- Gavazzi, G., Bonfanti, C., Sanvito, G., Boselli, A., & Scudeglio, M. 2002, ApJ, 576, 135
- Gonzalez, A. H., Zaritsky, D., & Wechsler, R. H. 2002, ApJ, 571, 129
- Ilbert, O., Arnouts, S., McCracken, H. J., et al. 2006, A&A, 457, 841
- Iovino, A., McCracken, H. J., Garilli, B., et al. 2005, A&A, 442, 423
- Kaiser, N. 1984, ApJ, 284, L9
- Lahav, O., Fabian, A. C., Edge, A. C., & Putney, A. 1989, MNRAS, 238, 881
- Landy, S. D. & Szalay, A. S. 1993, ApJ, 412, 64
- Le Fèvre, O., Guzzo, L., Meneux, B., et al. 2005a, A&A, 439, 877
- Le Fèvre, O., Vettolani, G., Garilli, B., et al. 2005b, A&A, 439, 845
- Le Fèvre, O., Vettolani, G., Paltani, S., et al. 2004, A&A, 428, 1043
- Limber, D. N. 1953, ApJ, 117, 134
- Lonsdale, C. J., Smith, H. E., Rowan-Robinson, M., et al. 2003, PASP, 115, 897
- Magliocchetti, M. & Maddox, S. J. 1999, MNRAS, 306, 988
- Maller, A. H., McIntosh, D. H., Katz, N., & Weinberg, M. D. 2005, ApJ, 619, 147
- Meneux, B., Le Fèvre, O., Guzzo, L., et al. 2006, A&A, 452, 387
- Norberg, P., Baugh, C. M., Hawkins, E., et al. 2002, MNRAS, 332, 827
- Oliver, S., Waddington, I., Gonzalez-Solares, E., et al. 2004, ApJS, 154, 30
- Pollo, A., Guzzo, L., Le Fèvre, O., et al. 2006, A&A, 451, 409
- Pollo, A., Meneux, B., Guzzo, L., et al. 2005, A&A, 439, 887

Postman, M., Huchra, J. P., & Geller, M. J. 1992, *ApJ*, 384, 404
 Roche, N., Shanks, T., Metcalfe, N., & Fong, R. 1993, *MNRAS*, 263, 360
 Rowan-Robinson, M., Babbedge, T., Surace, J., et al. 2005, *AJ*, 129, 1183
 Simpson, C. & Eisenhardt, P. 1999, *PASP*, 111, 691
 White, S. D. M. & Rees, M. J. 1978, *MNRAS*, 183, 341
 Zehavi, I., Zheng, Z., Weinberg, D. H., et al. 2005, *ApJ*, 630, 1
 Zucca, E., Ilbert, O., Bardelli, S., et al. 2006, *A&A*, 455, 879

¹ Laboratoire d'Astrophysique de Marseille, UMR 6110 CNRS-Université de Provence, BP8, 13376 Marseille Cedex 12, France

² INAF-Osservatorio Astronomico di Brera - Via Brera 28, Milan, Italy

³ Department of Astronomy, Cornell University, Space Sciences Building, Ithaca, NY 14853, USA

⁴ Infrared Processing & Analysis Center, California Institute of Technology, MS 100-22, Pasadena, CA 91125, USA

⁵ Center for Astrophysics & Space Sciences, University of California San Diego, La Jolla, CA 92093-0424, USA

⁶ IASF-INAF - via Bassini 15, I-20133, Milano, Italy

⁷ Astronomy Centre, University of Sussex, Brighton BN1 9QH, UK

⁸ INAF-Osservatorio Astronomico di Bologna - Via Ranzani, 1, I-40127, Bologna, Italy

⁹ IRA-INAF - Via Gobetti, 101, I-40129, Bologna, Italy

¹⁰ Spitzer Science Center, California Institute of Technology, Mail Stop 314-6, 1200 East California Boulevard, Pasadena, CA 91125, USA

¹¹ INAF-Osservatorio Astronomico di Capodimonte - Via Moiariello 16, I-80131, Napoli, Italy

¹² Università di Bologna, Dipartimento di Astronomia - Via Ranzani, 1, I-40127, Bologna, Italy

¹³ Laboratoire d'Astrophysique de l'Observatoire Midi-Pyrénées (UMR 5572) - 14, avenue E. Belin, F31400 Toulouse, France

¹⁴ Max Planck Institut fur Astrophysik, 85741, Garching, Germany

¹⁵ Institut d'Astrophysique de Paris, UMR 7095, 98 bis Bvd Arago, 75014 Paris, France

¹⁶ Observatoire de Paris, LERMA, 61 Avenue de l'Observatoire, 75014 Paris, France

¹⁷ Astrophysical Institute Potsdam, An der Sternwarte 16, D-14482 Potsdam, Germany

¹⁸ INAF-Osservatorio Astronomico di Roma - Via di Frascati 33, I-00040, Monte Porzio Catone, Italy

¹⁹ Università di Milano-Bicocca, Dipartimento di Fisica - Piazza delle Scienze, 3, I-20126 Milano, Italy

²⁰ Integral Science Data Centre, ch. d'Écogia 16, CH-1290 Versoix

²¹ Geneva Observatory, ch. des Maillettes 51, CH-1290 Sauverny, Switzerland

²² Astronomical Observatory of the Jagiellonian University, ul Orla 171, 30-244 Kraków, Poland

²³ Centre de Physique Théorique, UMR 6207 CNRS-Université de Provence, F-13288 Marseille France

²⁴ Centro de Astrofísica da Universidade do Porto, Rua das Estrelas, 4150-762 Porto, Portugal

²⁵ Institute for Astronomy, 2680 Woodlawn Dr., University of Hawaii, Honolulu, Hawaii, 96822

²⁶ School of Physics & Astronomy, University of Nottingham, University Park, Nottingham, NG72RD, UK